



## Determination of the fibre orientation distribution of a mineral wool network and prediction of its transverse stiffness using X-ray tomography

Chapelle, Lucie; Lyckegaard, Allan; Kusano, Yukihiro; Gundlach, Carsten; Foldschack, Mathilde Rosendahl; Lybye, Dorthe; Brøndsted, Povl

*Published in:*  
Journal of Materials Science

*Link to article, DOI:*  
[10.1007/s10853-018-2044-7](https://doi.org/10.1007/s10853-018-2044-7)

*Publication date:*  
2018

*Document Version*  
Early version, also known as pre-print

[Link back to DTU Orbit](#)

*Citation (APA):*  
Chapelle, L., Lyckegaard, A., Kusano, Y., Gundlach, C., Foldschack, M. R., Lybye, D., & Brøndsted, P. (2018). Determination of the fibre orientation distribution of a mineral wool network and prediction of its transverse stiffness using X-ray tomography. *Journal of Materials Science*, 53(9), 6390-6402. <https://doi.org/10.1007/s10853-018-2044-7>

---

### General rights

Copyright and moral rights for the publications made accessible in the public portal are retained by the authors and/or other copyright owners and it is a condition of accessing publications that users recognise and abide by the legal requirements associated with these rights.

- Users may download and print one copy of any publication from the public portal for the purpose of private study or research.
- You may not further distribute the material or use it for any profit-making activity or commercial gain
- You may freely distribute the URL identifying the publication in the public portal

If you believe that this document breaches copyright please contact us providing details, and we will remove access to the work immediately and investigate your claim.

Dear Author,

Here are the proofs of your article.

- You can submit your corrections **online**, via **e-mail** or by **fax**.
- For **online** submission please insert your corrections in the online correction form. Always indicate the line number to which the correction refers.
- You can also insert your corrections in the proof PDF and **email** the annotated PDF.
- For fax submission, please ensure that your corrections are clearly legible. Use a fine black pen and write the correction in the margin, not too close to the edge of the page.
- Remember to note the **journal title**, **article number**, and **your name** when sending your response via e-mail or fax.
- **Check** the metadata sheet to make sure that the header information, especially author names and the corresponding affiliations are correctly shown.
- **Check** the questions that may have arisen during copy editing and insert your answers/ corrections.
- **Check** that the text is complete and that all figures, tables and their legends are included. Also check the accuracy of special characters, equations, and electronic supplementary material if applicable. If necessary refer to the *Edited manuscript*.
- The publication of inaccurate data such as dosages and units can have serious consequences. Please take particular care that all such details are correct.
- Please **do not** make changes that involve only matters of style. We have generally introduced forms that follow the journal's style. Substantial changes in content, e.g., new results, corrected values, title and authorship are not allowed without the approval of the responsible editor. In such a case, please contact the Editorial Office and return his/her consent together with the proof.
- If we do not receive your corrections **within 48 hours**, we will send you a reminder.
- Your article will be published **Online First** approximately one week after receipt of your corrected proofs. This is the **official first publication** citable with the DOI. **Further changes are, therefore, not possible.**
- The **printed version** will follow in a forthcoming issue.

#### **Please note**

After online publication, subscribers (personal/institutional) to this journal will have access to the complete article via the DOI using the URL: [http://dx.doi.org/\[DOI\]](http://dx.doi.org/[DOI]).

If you would like to know when your article has been published online, take advantage of our free alert service. For registration and further information go to: <http://www.link.springer.com>.

Due to the electronic nature of the procedure, the manuscript and the original figures will only be returned to you on special request. When you return your corrections, please inform us if you would like to have these documents returned.

# Metadata of the article that will be visualized in OnlineFirst

---

ArticleTitle	Determination of the fibre orientation distribution of a mineral wool network and prediction of its transverse stiffness using X-ray tomography	
--------------	---	--

---

Article Sub-Title		
-------------------	--	--

---

Article CopyRight	Springer Science+Business Media, LLC, part of Springer Nature (This will be the copyright line in the final PDF)	
-------------------	---	--

---

Journal Name	Journal of Materials Science	
--------------	------------------------------	--

---

Corresponding Author	Family Name	<b>Chapelle</b>
	Particle	
	Given Name	<b>Lucie</b>
	Suffix	
	Division	
	Organization	ROCKWOOL International A/S
	Address	Group Development Hovedgaden 584, 2640, Hedehusene, Denmark
	Phone	
	Fax	
	Email	lucie.chapelle@rockwool.com
	URL	
	ORCID	<a href="http://orcid.org/0000-0002-9672-5596">http://orcid.org/0000-0002-9672-5596</a>

---

Author	Family Name	<b>Lyckegaard</b>
	Particle	
	Given Name	<b>Allan</b>
	Suffix	
	Division	
	Organization	Xnovo Technology ApS
	Address	Theilgaards Alle 9,1th, 4600, Køge, Denmark
	Phone	
	Fax	
	Email	
	URL	
	ORCID	

---

Author	Family Name	<b>Kusano</b>
	Particle	
	Given Name	<b>Yukihiro</b>
	Suffix	
	Division	Department of Wind Energy
	Organization	Technical University of Denmark
	Address	Risø Campus, Frederiksborgvej 399, 4000, Roskilde, Denmark
	Phone	
	Fax	
	Email	
	URL	

ORCID

---

Author	Family Name	<b>Gundlach</b>
	Particle	
	Given Name	<b>Carsten</b>
	Suffix	
	Division	Department of Physics
	Organization	Technical University of Denmark
	Address	Fysikvej, 2800, Kgs. Lyngby, Denmark
	Phone	
	Fax	
	Email	
	URL	
	ORCID	

---

Author	Family Name	<b>Foldschack</b>
	Particle	
	Given Name	<b>Mathilde Rosendahl</b>
	Suffix	
	Division	
	Organization	ROCKWOOL International A/S
	Address	Group Development Hovedgaden 584, 2640, Hedehusene, Denmark
	Phone	
	Fax	
	Email	
	URL	
	ORCID	

---

Author	Family Name	<b>Lybye</b>
	Particle	
	Given Name	<b>Dorthe</b>
	Suffix	
	Division	
	Organization	ROCKWOOL International A/S
	Address	Group Development Hovedgaden 584, 2640, Hedehusene, Denmark
	Phone	
	Fax	
	Email	
	URL	
	ORCID	

---

Author	Family Name	<b>Brøndsted</b>
	Particle	
	Given Name	<b>Povl</b>
	Suffix	
	Division	Department of Wind Energy
	Organization	Technical University of Denmark
	Address	Risø Campus, Frederiksborgvej 399, 4000, Roskilde, Denmark
	Phone	

Fax  
Email  
URL  
ORCID

---

Schedule	Received	25 October 2017
	Revised	
	Accepted	16 January 2018

---

Abstract

A method to determine the orientation and diameter distributions of mineral wool fibre networks using X-ray tomography and image analysis is presented. The method is applied to two different types of mineral wool: glass wool and stone wool. The orientation information is obtained from the computation of the structure tensor, and the diameter is estimated by applying a greyscale granulometry. The results of the image analysis indicate the two types of fibres are distributed in a 2D planar arrangement with the glass wool fibres showing a higher degree of planarity than the stone wool fibres. The orientation information is included in an analytical model based on a Euler–Bernoulli beam approximation. The model enables prediction of the transverse stiffness. It is indicated that the glass wool transverse stiffness is lower than the stone wool transverse stiffness. Comparison with experimental results confirms the assumption that the underlying deformation mechanism of mineral wool is the bending of fibre segments between bonds.

---

Footnote Information

---

_2D materials	_EBSD	_materials design	_resorbable materials
_ab initio calculations	_elastic properties	_materials for demanding environments	_responsive materials
_additive manufacturing	_electrical properties	_materials for energy	_rheology
_adhesion	_electrocatalysis	_mechanical properties	_sapphire/Al <sub>2</sub> O <sub>3</sub>
_adsorption	_electrochemistry	_membranes	_scaffolds
_aerogels	_electrode materials	_mesoporous materials	_scanned-probe microscopy
_AFM	_electron-beam melting	_metal-insulator transition	_selective laser melting
_alloys	_electronic materials	_metal/organic frameworks (MOFs)	_self-assembly
_amorphous materials	_electronic properties	_metallic glasses	_self-healing materials
_annealing	_electrospinning	_metals	_SEM
_antifouling materials	_embrittlement	_metamaterials	_semiconductors
_atomic-layer deposition (ALD)	_energy harvesting	_microanalysis	_sensing and sensors
_atomistic modeling	_epitactic or epitaxial growth	_microstructure	_severe plastic deformation
_batteries	_fatigue	_minerals or mineralization	_shape memory materials
_batteries, lithium	_FCC metals	_molding	_silicones
_batteries, magnesium	_ferroelectrics	_molecular dynamics	_singlet-exciton fission
_batteries, sodium	_FGMs	_molecular simulation	_sintering
_BCC metals	_fibers or fiber technology	_molecular-beam epitaxy (MBE)	_small volume testing
_bio-inspired materials	_food colloids	_morphology	_smart materials
_biomass conversion	_fracture	_multiferroics	_sodium-sulphur batteries
_biomaterials	_fuel cells	_multilayers	_soft interfaces
_biomechanics	_functional anisotropy	_nanocomposites	_soft matter
_biomimetic	_functional materials	_nanofunctionality	_sol-gel preparation
_black phosphorus	_gas-phase transport	_nanoindentation	_solidification
_blends	_gelation	_nanolithography	_solvothermal/hydrothermal
_brazing	_geocomposites	_nanomaterials	_spectroscopy (XPS)
_calcification	_glass	_nanomedicines	_spin glass
_capacitors	_grain boundaries	_nanoporous materials	_spintronics
_carbon fiber	_grain boundary engineering	_natural materials	_sputter deposition
_carbon nanotube	_graphene	_NDT	_STM
_casting	_graphitic carbon	_NMR	_superalloys
_catalysts or catalysis	_hardness	_nuclear materials	_supercapacitors
_cellular materials	_HCP metals	_nucleation	_superconductors
_cellulose	_healing	_omniphobic materials	_superelasticity
_ceramics	_heat treatment	_optical materials and properties	_superhydrophobic
_characterization methods	_hierarchical materials	_organic electronics	_surface treatments
_chemical vapor deposition (CVD)	_high entropy alloys	_organic solar-cell materials	_surfaces
_CO <sub>2</sub> sequestration	_high pressure torsion	_permeable materials	_surfactants
_coatings	_high throughput testing	_perovskite	_technical textiles
_colloids or bio-colloids	_hot isostatic pressing	_perovskite solar cell (PSCs)	_TEM
_composite materials	_hydrogels	_phase diagrams	_texture
_computational materials science	_hydrogen storage or production	_phase transformations	_theranostics
_computer modeling	_hydrolysis	_phase-change materials (PCMs)	_thermal barrier coatings
_computer simulation	_II-VI compounds	_phase-field modeling	_thermal properties
_conducting polymers	_III-V compounds	_phosphors	_thermodynamics
_corrosion and oxidation	_imaging	_photocatalysis	_thermoelectrics
_corrosion protection	_In situ or operando	_photonic materials	_thin-film or thick-film coatings
_crystal plasticity	_infrared spectroscopy	_photoreactive materials	_TiO <sub>2</sub> rutile, anatase or brookite
_crystallization	_intercalation	_phototherapeutics	_tissue engineering
_curing	_interfaces	_photovoltaics (solar cells)	_tomography
_data analytics	_intermetallics	_piezoelectric materials	_topological insulators
_defects	_ionomers	_plasma deposition	_transparent conductors
_deformation	_kinetics	_plasmonic materials	_transport mechanisms
_deposition	_laminates	_plating	_tribology
_dielectrics	_laser processing	_polymers	_twinning
_diffraction, electron	_latticed effects	_porous materials	_TWIP steels
_diffraction, neutron	_layered materials	_powder technology	_two-photon adsorption
_diffraction, X-ray (XRD)	_light alloys	_pyroelectrics	_UFG materials
_diffusion	_light-emitting diodes	_quasicrystals	_viscoelasticity
_diodes	_liquid crystals	_radiation damage	_viscosity
_dislocation dynamics	_lithography	_radiation effects	_water-splitting
_dislocations	_machining	_rapidly solidified materials	_wear
_drug delivery	_macro defects	_redox flow batteries	_wood
_dye-sensitized solar cells (DSSCs)	_magnetic materials or properties	_regenerative medicine	_XPS
_dysfunctional materials	_magnetic ordering		_zeolite



# Determination of the fibre orientation distribution of a mineral wool network and prediction of its transverse stiffness using X-ray tomography

Lucie Chapelle<sup>1,\*</sup> , Allan Lyckegaard<sup>2</sup>, Yukihiro Kusano<sup>3</sup>, Carsten Gundlach<sup>4</sup>, Mathilde Rosendahl Foldschack<sup>1</sup>, Dorthe Lybye<sup>1</sup>, and Povl Brøndsted<sup>3</sup>

<sup>1</sup>ROCKWOOL International A/S, Group Development Hovedgaden 584, 2640 Hedehusene, Denmark

<sup>2</sup>Xnovo Technology ApS, Theilgaard Alle 9, 1th, 4600 Køge, Denmark

<sup>3</sup>Department of Wind Energy, Technical University of Denmark, Risø Campus, Frederiksborgvej 399, 4000 Roskilde, Denmark

<sup>4</sup>Department of Physics, Technical University of Denmark, Fysikvej, 2800 Kgs. Lyngby, Denmark

Received: 25 October 2017

Accepted: 16 January 2018

© Springer Science+Business Media, LLC, part of Springer Nature 2018

## ABSTRACT

A method to determine the orientation and diameter distributions of mineral wool fibre networks using X-ray tomography and image analysis is presented. The method is applied to two different types of mineral wool: glass wool and stone wool. The orientation information is obtained from the computation of the structure tensor, and the diameter is estimated by applying a greyscale granulometry. The results of the image analysis indicate the two types of fibres are distributed in a 2D planar arrangement with the glass wool fibres showing a higher degree of planarity than the stone wool fibres. The orientation information is included in an analytical model based on a Euler–Bernoulli beam approximation. The model enables prediction of the transverse stiffness. It is indicated that the glass wool transverse stiffness is lower than the stone wool transverse stiffness. Comparison with experimental results confirms the assumption that the underlying deformation mechanism of mineral wool is the bending of fibre segments between bonds.

## Introduction

Mineral wool designates the fibrous materials obtained by spinning or drawing mineral melts. Three types of mineral wool exist: stone wool produced from volcanic rocks, glass wool whose raw materials include sand and recycled glass and slag wools obtained from the recycled products of blast

furnaces. Among them, stone wool and glass wool materials are important due to the extensive use as thermal insulators in buildings. The compression behaviour is of interest as both materials experience compressive stresses during for example packing and transport. At low compressive strains, both materials present a linear elastic behaviour. Currently, the literature is rather limited on this subject. The

Address correspondence to E-mail: lucie.chapelle@rockwool.com

55 compressive behaviour of stone wool has been  
 56 studied in [1] but only in the nonlinear elastic regime  
 57 under compressive strains up to 95%. To improve the  
 58 compression properties of mineral wool products, an  
 59 understanding of the relationship between the  
 60 macroscopic linear elastic deformation of mineral  
 61 wool and the underlying single fibre behaviour and  
 62 fibre network structure is required. The characteri-  
 63 zation of the fibre network structure is needed to  
 64 explore this relationship.

65 The methods and tools for the characterization of  
 66 mineral wool are based on the analysis of 3D datasets  
 67 obtained by X-ray computed tomography (X-ray CT).  
 68 High-resolution X-ray CT has gained considerable  
 69 importance in the examination and 3D-characteriza-  
 70 tion of materials and industrial specimens in the last  
 71 decade [2–7]. Analysis of the X-ray CT data can  
 72 provide important microstructural characteristics, for  
 73 example, the orientation and the diameter distribu-  
 74 tions of the fibres. For sub-micrometre resolution, an  
 75 X-ray synchrotron set-up is usually needed. How-  
 76 ever, in the recent years the technology has evolved  
 77 to the point where laboratory X-ray sources and  
 78 optics are also able to produce data with sub-mi-  
 79 crometre resolution. In the field of textile research,  
 80 where fibres are a part of the structure, the yarn fibre  
 81 direction has been estimated from the analysis of 3D  
 82 X-ray micro-CT data [8–13]. Vigiúí et al. [14] pro-  
 83 posed a method for labelling and identifying contact  
 84 points of 3D datasets and Eberhardt and Clarke  
 85 introduced a technique to trace fibres in 3D datasets  
 86 of composites and textiles materials. The same tech-  
 87 nique is later implemented by Tausif et al. to measure  
 88 the orientation of segments of fibres in nonwovens  
 89 materials [15, 16]. The complex structure of the fibre  
 90 network in paper material has also been investigated  
 91 by X-ray CT in several studies. These include studies  
 92 of application of microtomography to paper [17],  
 93 fibre twist and aspect ratio [18], paper anisotropy and  
 94 heterogeneity using covariograms [19] and analysis  
 95 of the microstructure under different manufacturing  
 96 conditions [20, 21]. 3D X-ray micro-CT of stone wool  
 97 has been used for measuring the displacement field  
 98 during deformation [22, 23]. The deformation of the  
 99 imaged sample of stone wool was correlated to its  
 100 local density variations, but no other quantifications  
 101 were conducted. To obtain information about the  
 102 orientation distribution of the fibres, most image  
 103 analysis techniques require an individual fibre seg-  
 104 mentation as a prior step [24, 25]. For complex fibre

networks such as mineral wool, individual fibre  
 segmentation can be difficult and computationally  
 expensive.

Several studies have addressed the linear elastic  
 properties of random networks, interpreted as solid  
 networks or cellular structure. One of the earliest  
 contributions, the analytical model of Gibson et al.  
 [26] developed for foams expresses the macroscopic  
 moduli of cellular materials as power laws in terms of  
 the relative density. It has been applied for fibres  
 network in [27] for stainless steel fibres, carbon fibres  
 and glass fibres network cross-linked with epoxy.  
 Clyne et al. [28] have also presented a simple ana-  
 lytical model to predict the stiffness of metallic bon-  
 ded fibres. These models assume that the fibre  
 orientation distribution of the networks is either 2D  
 random or 3D random. In summary, the existing  
 characterization methods do not satisfactorily pro-  
 vide information needed for study of deformation  
 mechanics. In addition, fibre network models repor-  
 ted in the literature should be further developed for  
 more realistic representation of 3D elastic behaviour  
 of fibre network. To develop an understanding of the  
 mechanisms of deformation during compression, we  
 propose here a methodology to characterize the  
 structure of fibrous materials and derive an analytical  
 model to estimate the transverse stiffness of the  
 mineral wool networks using the results of the  
 characterization. As there are currently no dedicated  
 tools for the 3D characterization of mineral wool  
 fibres network, we have implemented our own image  
 analysis tools relying on the structure tensor to  
 extract the fibre orientation information and using  
 greyscale morphology to access the fibre diameter  
 distribution. It is important to note that in this work  
 the individual fibre segmentation is not a prerequisite  
 for the estimation of the fibre orientation and diam-  
 eter distribution. The methodology and model are  
 applied to glass wool and stone wool products to  
 study the differences at the fibre network scale  
 between the two. The model we propose here can  
 deal with every type of orientation distribution of the  
 fibres. Indeed, the aim of the present paper is to  
 quantify the fibre orientation and diameter of a glass  
 wool and stone wool sample using image analysis of  
 high-resolution X-ray CT and use the obtained char-  
 acteristics as inputs in a simple analytical model  
 predicting the transverse stiffness. Acquisition  
 parameters for the X-ray CT, pre-processing of the  
 datasets and details on the image analysis algorithms

155 and modelling approach are outlined in the [Materials](#)  
 156 [and methods](#) section below. Results of the images  
 157 analysis and modelling for both types of mineral  
 158 wool are compared, and the findings are discussed in  
 159 the [Results and discussion](#) section.

160 **Materials and methods**

161 **Materials**

162 The mineral wool fibres studied are discontinuous  
 163 glass fibres with a typical diameter of 2 to 6 microme-  
 164 tres and a length varying from millimetre to centimetre  
 165 scale. There are three types of industrially important  
 166 mineral wool: slag wool, glass wool and stone wool.  
 167 This study is focussing on stone wool and glass wool,  
 168 and therefore, only their production process will be  
 169 shortly described here. Stone wool fibre is normally  
 170 produced by a centrifuge process known as cascade  
 171 spinning where droplets of melts are drawn into fibres  
 172 by centrifugal forces. During the drawing of stone  
 173 wool fibres some of the spherical droplets known in the  
 174 industry as shots stay inside the final product. The  
 175 glass wool fibres are obtained by pouring melt into a  
 176 spinning cup. The fibres are drawn by centrifugal  
 177 forces, but no shots are formed during this process.  
 178 Binder and refined mineral oil are added to make the  
 179 material both mechanically stable and water repellent.  
 180 Subsequently, the stone wool and glass wool fibres  
 181 networks are heated in order to cure the binder. The  
 182 binder creates the bonds between the fibres and gives  
 183 dimensional stability to the final board. The samples  
 184 chosen for this study are taken from a semi-rigid  
 185 insulation board commercialized under the name  
 186 ROCKWOOL Flexibatts® with a density of approxi-  
 187 mately 34 kg/m<sup>3</sup> and a glass wool insulation batt  
 188 commercialized under the name Isover Flex® with a  
 189 density of approximately of 22 kg/m<sup>3</sup>. Subsequently,  
 190 we will refer to the two materials as stone wool and  
 191 glass wool.

192 **Image acquisition and pre-processing**

193 The data used in this paper are acquired on a labo-  
 194 ratory scanner, ZEISS Xradia 410 Versa with a reso-  
 195 lution of 1–50 μm in samples of size 1–50 mm. Details  
 196 of the image acquisition and obtained voxel size for  
 197 the sample of glass wool and stone wool are pre-  
 198 sented in Table 1.

**Table 1** Parameters for data acquisition

	Energy (keV)	Objective	Exposure time (s)	Voxel size (μm)
Glass wool	80	10×	4.0	1.71
Stone wool	80	20×	10.0	0.87

A different objective and thus magnification was used for the glass wool sample because of its low fibre density. The reconstructed image data contain noise due to a number of factors, e.g. artefacts from the reconstruction algorithm, differences in the absorption coefficients of the materials and detector noise. A pre-processing step may therefore be needed to reduce the effect of the noise on the further analysis. Linear filters, e.g. Gaussian filters, will blur the edges, which might lead to an overestimation of the size of the objects. For that reason, a median filter is used to pre-process the images.

**Orientation analysis**

The changes of orientation in an image are indicated by intensity variations. The first-order intensity variation is the gradient. To define the direction, a global framework is needed. However, most of the image operations to analyse direction are locally based. Therefore, to obtain the main orientation, one must average the local orientation and ensure that gradient vectors pointing in opposite directions do not cancel out but enhance each other. The gradient structure tensor, first introduced by Bigun et al. [29], overcomes this problem by computing the local gradient in a quadratic form. The structure tensor has successfully been used for object tracking, texture segmentation, flow estimation as well as orientation of complex patterns such as fingerprints [30–33].

The gradient structure tensor is a tensor representation of the inner product of the partial derivatives of the image. The gradient structure tensor is defined as:

$$J(x, y, z) = \begin{bmatrix} \langle f_x, f_x \rangle_\rho & \langle f_x, f_y \rangle_\rho & \langle f_x, f_z \rangle_\rho \\ \langle f_y, f_x \rangle_\rho & \langle f_y, f_y \rangle_\rho & \langle f_y, f_z \rangle_\rho \\ \langle f_z, f_x \rangle_\rho & \langle f_z, f_y \rangle_\rho & \langle f_z, f_z \rangle_\rho \end{bmatrix} \quad (1)$$

where  $f_i$  is the derivative of the image  $f$  in the direction  $i$  and the weighted inner product between two images  $g$  and  $h$  is defined as:

Author Proof

$$\langle g, h \rangle_\rho = K_\rho * (g \cdot h) \quad (2)$$

236 where \* denotes the convolution operator,  $\cdot$  represents the inner product, and  $K_\rho$  is the Gaussian  
 237 weighting function that averages the orientation  
 238 within a neighbourhood. The integration scale  $\rho$   
 239 should reflect the characteristic size of the texture  
 240 considered. Once the structure tensor has been  
 241 obtained for each voxel over a neighbourhood  
 242 defined by the scale  $\rho$ , the eigenvalues and eigen-  
 243 vectors are determined. We assume that the eigen-  
 244 values are ordered, i.e.  $\lambda_i \geq \lambda_{i+1}$ . The eigenvector  $e_3$   
 245 corresponds to the smallest eigenvalue  $\lambda_3$  and hereby  
 246 corresponds to the orientation with the lowest fluctu-  
 247 ations. For voxels belonging to a fibre, this will give  
 248 the orientation of the fibre locally. The eigenvectors  
 249 and the eigenvalues relate to the structure present in  
 250 the image. The orientation of the eigenvector  $e_3$  can be  
 251 described by two angles, the elevation angle  $\theta$  and the  
 252 azimuth angle  $\varphi$  as follows:  
 253

$$e_3 = \begin{Bmatrix} e_x \\ e_y \\ e_z \end{Bmatrix} = \begin{Bmatrix} \cos \theta \cos \varphi \\ \cos \theta \sin \varphi \\ \sin \theta \end{Bmatrix}, \theta \in [0, \pi], \varphi \in [0, \pi] \quad (3)$$

255 To present and interpret the results dealing with the  
 256 orientation information of the fibres, the elevation  
 257 and azimuthal angles will be used. The following  
 258 conventions are adopted with respect to the axis  
 259 system: the  $z$  axis represents the thickness direction  
 260 of the mineral wool sample. The angle  $\theta$  is the angle  
 261 between the  $z$  axis and the fibre direction. The angle  
 262  $\varphi$  measures the angle between the axis  $x$  and the  
 263 projection of the fibre direction in the  $x$ - $y$  plane.

### 264 Implementation details

265 The computation of the structure tensor and the cal-  
 266 culation of the eigenvectors are written in MATLAB.  
 267 The image partial derivatives are obtained by con-  
 268 **AQ2**volving the input image with Scharr kernel [34].  
 269 Scharr operators are recognized as more accurate  
 270 than other common derivative operators. Once the  
 271 structure tensor is obtained, the eigenvalues and the  
 272 eigenvector are calculated using an analytical  
 273 expression so that the code is vectorized and to avoid  
 274 looping over all the voxels of the image.

### Diameter analysis

276 The diameter distribution of the fibres is estimated  
 277 using grey-level morphological granulometry, which  
 278 has several advantages compared to the binary  
 279 counterpart [35]. A granulometry is a sequence of  
 280 openings with convex structuring elements of  
 281 increasing size that simulates a sieving procedure  
 282 with increasing mesh width. Distribution of dimen-  
 283 sions in an image can be obtained by granulometry.  
 284 The majority of the granulometry methods in the  
 285 literature requires the conversion of the greyscale  
 286 image into binary. For example, binary granulometry  
 287 was successfully applied to medium density fibre-  
 288 board (MDF) to determine the size distribution of  
 289 fibres and sometimes of pores [36–39]. However,  
 290 during the conversion from greyscale to binary im-  
 291 ages, some of the information is lost. For example, the  
 292 voxels corresponding to the edge of the fibre are  
 293 either set to the background or to the fibre and this  
 294 will lead to errors in the estimation of the fibre  
 295 diameter. It is therefore advantageous to work on  
 296 greyscale images rather than binary when determin-  
 297 ing the fibre diameter in images with a low  
 298 resolution.

299 For each voxel  $p$  of a greyscale image  $I$ , we can  
 300 define the pattern spectrum of a granulometry  
 301  $PS_{\gamma_n}(p)$  as:

$$\forall n > 0, PS_{\gamma_n}(p) = \varphi(\psi_n(I(p))) - \varphi(\psi_{n-1}(I(p))) \quad (4)$$

303 where  $\psi_n$  is an opening with a structuring element of  
 304 size  $n$  and  $\varphi$  is a measure function.

305 For example for a greyscale image, the measure  
 306 function  $\varphi$  can simply be the intensity of the voxel. If  
 307 the structuring element is a ball of radius  $n$ , the pat-  
 308 tern spectrum carries information about the distri-  
 309 bution of the diameter of the fibres. Commonly, the  
 310 size of the object at a voxel  $d(p)$  is expressed as the  
 311 scale for which the pattern spectrum reaches its  
 312 maximal value:

$$d(p) = \arg \max_n (PS_{\gamma_n}(p)) \quad (5)$$

314 However, for greyscale granulometry different max-  
 315 imum values can be reached at different scales. To  
 316 take this effect into account, the methodology pre-  
 317 sented in [35] by Moreno and co-workers is adopted:  
 318 the size of an object is computed as a combination of  
 319 the values of the pattern spectrum at different scales.  
 320 They also include in the expression for the size of an  
 321 object a parameter to correct the bias induced by the

322 edge effect: the intensity of the voxels at the fibre  
 323 edges reflects the fact that the edges are a mixture of  
 324 the fibre and the background. Therefore, they should  
 325 contribute less to the measure of the diameter. The  
 326 resulting expression obtained by Moreno et al. for the  
 327 size of an object at a voxel  $p$  belonging to  $I$ ,  $d(p)$  is:

$$d(p) = 2 \frac{\sum nPS_{\gamma_n}(p)}{\sum PS_{\gamma_n}(p)} - \frac{M - I(p)}{M - m} \quad (6)$$

329 with  $M$  and  $m$  being the maximum and minimum  
 330 intensities of the image  $I$ , respectively.

331 **Implementation details**

332 The greyscale granulometry method is implemented  
 333 in MATLAB. Looping over the size of the structural  
 334 element and the pattern spectrum is obtained by  
 335 opening the image with the structural element built  
 336 according to the recommendations presented in [35].

337 **Analytical model**

338 To estimate the transverse stiffness of the mineral  
 339 wool fibre network, the deflection of a single fibre  
 340 segment under uniaxial compressive load in the  $z$   
 341 direction is considered. The single fibre segment can  
 342 be represented by a Euler–Bernoulli beam clamped at  
 343 both ends and submitted to a concentrated load in its  
 344 centre. The clamped ends of the fibre segment model  
 345 the bonds of the mineral wool fibre network that we  
 346 consider rigid in this first modelling approach. Under  
 347 these conditions, the transverse deflection of the  
 348 beam  $\delta$  can be expressed as follows:

$$\delta = \frac{\Delta z}{\sin \theta} = \frac{W \sin \theta L^3}{3E_f \pi D^4} \quad (7)$$

350  $\Delta z$  is the deflection in the  $z$  direction,  $W$  is the  
 351 concentrated load applied at the middle of the fibre  
 352 segment,  $L$  is the mean fibre segment length (i.e. the  
 353 mean length between two bonds),  $E_f$  is the Young's  
 354 modulus of the fibre,  $D$  is the mean fibre diameter,  
 355 and  $\theta$  is the elevation angle defined earlier. Figure 1  
 356 gives the definition of the different variables.

357 The strain in the  $z$  direction can be expressed as the  
 358 ratio of the transverse deflection over the initial  
 359 height projected by the fibre onto the  $z$  axis:

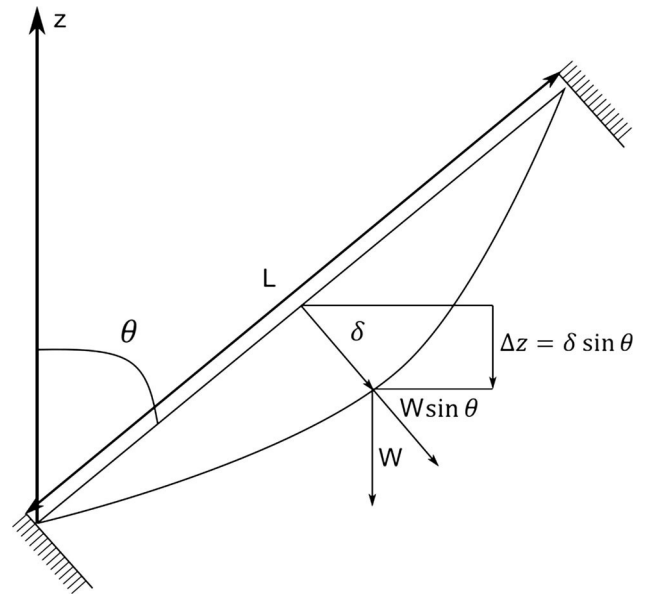


**Figure 1** Deflection of a single fibre segment under a concentrated load.

$$\varepsilon = \frac{\Delta z}{z} = \frac{W \sin^2 \theta L^2}{3 \cos \theta E_f \pi D^4} \quad (8)$$

This gives the following expression for the concentrated load applied to the fibre: 361 362

$$W = \frac{3\varepsilon \cos \theta E_f \pi D^4}{\sin^2 \theta L^2} \quad (9)$$

The applied stress  $\sigma$  to the mineral wool network 364 generates the load  $W$  on each individual fibre seg- 365 ment. These two quantities are related by: 366

$$\sigma = \int_0^\pi \int_0^\pi N_{fA} W d\theta d\varphi \quad (10)$$

where  $N_{fA}$  is the number of fibre segments per unit 368 sectional area. In that case, the unit area is the area 369 with a director parallel to the  $z$  axis. 370

The number of fibre segments per unit sectional 371 area  $N_{fA}$  was derived by Komori and Makishima [40] 372 as: 373

$$N_{fA} = N_{fV} I_f \Omega(\Theta, \psi) \Upsilon(\Theta, \psi) \quad (11)$$

where 375

$$\Upsilon(\Theta, \psi) = \int_0^\pi \int_0^\pi |\cos \chi| \Omega(\theta, \varphi) \sin \theta d\theta d\varphi \quad (12)$$

The angles  $\Theta, \psi$  give the orientation of the plane 377 considered for the unit sectional area. And the 378 quantity  $N_{fV}$  represents the total number of fibres 379

Author Proof

380 contained in the unit volume with mean fibre length  $l_f$   
381 and fibre volume fraction  $f$ :

$$N_{fV} = \frac{4f}{l_f \pi D^2} \quad (13)$$

383 The function  $\Omega(\theta, \varphi)$  is the probability density func-  
384 tion of the fibre orientation distribution. It is sub-  
385 mitted to the normalization condition:

$$\int_0^\pi \int_0^\pi \Omega(\theta, \varphi) \sin \theta \, d\theta \, d\varphi = 1 \quad (14)$$

387 In the case studied here, the unit sectional area has  
388 the axis  $z$  as a normal vector. The expression for the  
389 average number of fibre segments per unit sectional  
390 area then becomes:

$$N_{fA} = N_{fV} l_f \Omega(\theta, \varphi) \cos \theta = \frac{4f}{\pi D^2} \Omega(\theta, \varphi) \cos \theta \quad (15)$$

392 Replacing Eqs. 15 in 10 and averaging over all the  
393 possible fibre orientations  $(\theta, \varphi)$  yields to:

$$\sigma = \frac{12E_f f \varepsilon}{\left(\frac{L}{B}\right)^2} \int_0^\pi \int_0^\pi \frac{\cos^2 \theta}{\sin \theta} \Omega(\theta, \varphi) \, d\theta \, d\varphi \quad (16)$$

395 The transverse stiffness can be identified as:

$$E_{zz}^* = \frac{12E_f f}{\left(\frac{L}{B}\right)^2} \int_0^\pi \int_0^\pi \frac{\cos^2 \theta}{\sin \theta} \Omega(\theta, \varphi) \, d\theta \, d\varphi \quad (17)$$

397 The only unknown in the above expression is the  
398 mean fibre segment length as the other variables  
399 relating to the orientation distribution and the mean  
400 diameter of the fibres can be estimated experimen-  
401 tally using the methods described earlier. To evaluate  
402 this quantity, we use the model developed by Komori  
403 and Makishima [41] giving the mean number of fibre  
404 contact points in fibrous materials. The mean distance  
405 between fibre contact points is given by:

$$L = \frac{\pi D}{8If} \quad (18)$$

$$I = \int_0^\pi \int_0^\pi J(\theta, \varphi) \Omega(\theta, \varphi) \sin \theta \, d\theta \, d\varphi \quad (19)$$

$$J(\theta, \varphi) = \int_0^\pi \int_0^\pi \Omega(\theta, \varphi) \sin \chi \sin \theta \, d\theta' \, d\varphi' \quad (20)$$

$$\sin \chi = \left(1 - (\cos \theta \cos \theta' + \sin \theta \sin \theta' \cos(\varphi - \varphi'))\right)^{1/2} \quad (21)$$

413  $J(\theta, \varphi)$  is the mean angle between the fibres, while  
414  $\sin \chi$  is the angle between two arbitrary fibres and  $I$  a  
415 factor reflecting the fibre orientation.

Replacing the expression of the mean distance 416  
between fibre contact points in Eq. (17) yields to: 417

$$E_{zz}^* = \frac{3E_f l_f^2 f^3}{16\pi^2} \int_0^\pi \int_0^\pi \frac{\cos^2 \theta}{\sin \theta} \Omega(\theta, \varphi) \, d\theta \, d\varphi \quad (22)$$

In the model derived here, the final expression for the 419  
transverse modulus is only a function of the orien- 420  
tation of the segment of fibres, the fibre Young's 421  
modulus and its volume fraction. 422

## Experimental determination 423 of the transverse compression modulus 424

The compression testing of the specimens was 425  
determined according to the requirements of EN 826 426  
(1996). The compression speed is adjusted to 427  
 $d/10$  mm per minute (where  $d$  means the thickness 428  
of the test specimens in mm). The test specimen is 429  
compressed uniaxially in the thickness direction at a 430  
constant speed, and the force/deformation curve is 431  
recorded. The stress/strain curve is obtained, and the 432  
initial linear elastic part is used to determine the 433  
compression modulus. The test is performed on 434  
specimens with a thickness corresponding to the 435  
initial product thickness (100 mm for glass wool and 436  
140 mm for stone wool) and cut to a width of 100 and 437  
a length of 100 mm. The test is conducted on two 438  
specimens for each type of mineral wool. 439

## Results and discussion 440

### Fibre volume fraction and Young's modulus 441

The theoretical densities of the fibres are calculated 442  
based the chemical composition of the mineral wool 443  
fibres. The fibre volume fraction is estimated using 444  
the ratio of the product density over the fibre density. 445  
For the stone wool material, the fibre volume fraction 446  
is calculated considering that the material contains a 447  
weight fraction of 24.6% of shots. The theoretical 448  
Young's moduli of the glass wool and stone wool 449  
fibres are calculated according to the equation pre- 450  
sented in [42]: 451

$$E_f = 83.6V_t \sum G_i X_i \quad (23)$$

where  $V_t$  is the packing density,  $G_i$  the dissociation 453  
energy of the  $i$ th oxide, and  $X_i$  is the mole fraction of 454  
component  $i$  of an oxide glass. The packing density 455  
and dissociation energies are listed in [42]. The 456

457 parameters obtained from the references and used  
458 here are overall averages.

459 The results are listed in Table 2.

## 460 Fibre orientation distribution

461 The orientation information of the two fibre networks  
462 is extracted from the eigenvectors of the structure  
463 tensor. Because each voxel belonging to the fibre  
464 contains the orientation information, the distributions  
465 obtained are volume weighed. The orientation of the  
466 fibre network is described by the variations of the  
467 azimuthal and elevation angles. The histograms of  
468 the elevation angles and the polar plots of the azi-  
469 muth angles are given in Fig. 2. Both distributions of  
470 the elevation angles present a peak at approximately  
471  $90^\circ$  showing that the two networks have a preferen-  
472 tially laminar structure. The histogram of the glass  
473 wool fibre network exhibits a narrower distribution  
474 than the one observed in the stone wool material  
475 indicating a higher degree of laminar arrangement of  
476 the glass wool fibres. The polar histograms of the  
477 azimuth angles of the glass wool fibres network show  
478 that a high density of fibres oriented with an azi-  
479 muthal angle of  $\pi/6$ . On the other hand, the polar  
480 plot of the stone wool azimuthal angles indicates  
481 more uniformity in the distribution of the angles and  
482 thus a slightly higher degree of isotropy of the stone  
483 wool fibres in the  $x$ - $y$  plane.

484 A 3D rendering of the two materials is shown in  
485 Figs. 3 and 4. The colour scale of the image represents  
486 the variations of the azimuthal and elevation angles  
487 used to describe the local orientation information of a  
488 fibre. The renderings corroborate the analysis of the  
489 histograms plots: the colour of the 3D data repre-  
490 senting the variations of the elevation reflects that the  
491 majority of the fibres are contained in the  $x$ - $y$  plane.  
492 The 3D renderings show that for both materials, some  
493 of the fibres are arranged in a tuft: they are oriented  
494 in the same direction and located at a short distance  
495 from each other.

**Table 2** Fibre characteristics

	Glass wool	Stone wool
Fibre density ( $\text{kg/m}^3$ )	2554	2840
Fibre volume fraction (%)	0.86	0.90
Fibre Young's modulus (GPa)	70.32	99.12

## Fibre diameter distribution

497 To evaluate the performance of the greyscale granu-  
498 lometry, the distributions are compared to distribu-  
499 tions obtained from 2D measurements of the fibre  
500 diameter in the SEM according to the protocol pre-  
501 sented in [43]. Three samples are extracted from each  
502 of the two products, and the fibres are chopped,  
503 mixed in a solution with water and filtered through a  
504 membrane. The membrane is then fixed to a micro-  
505 scopy stub. Two stubs are prepared for each mineral  
506 wool. If the difference between the mean fibre  
507 diameters obtained for each stub is superior to  
508  $0.5 \mu\text{m}$ , then two additional stubs are prepared and  
509 measured. For the samples examined in this paper,  
510 this was not necessary. As the distribution of the  
511 fibres diameter given by the greyscale granulometry  
512 is volume weighted and the SEM based are length  
513 weighted, the obtained diameter distributions are  
514 transformed into a length weighted distribution by  
515 taking the value of the thickness of the fibres at their  
516 medial axis. The distribution obtained from the glass  
517 wool sample has a mode located at approximately  
518  $6 \mu\text{m}$ , while the distribution of the stone wool fibres  
519 reveals one peak located at approximately  $5 \mu\text{m}$ . By  
520 comparison to the SEM-based method, the greyscale  
521 granulometry fails to measure the thinnest fibres,  
522 especially for the glass wool dataset with the largest  
523 voxel size. Thus, the mean diameters returned by the  
524 measurements on the 3D datasets are  $1$ – $2 \mu\text{m}$  higher  
525 than the mean diameters obtained by the SEM  
526 method. The SEM measurements indicate that the  
527 glass wool and stone wool fibres follow a log-normal  
528 distribution with a similar mean diameter, but the  
529 shoulder of the distribution towards large diameters  
530 is broader for the glass wool fibres (Fig. 5).

## Modelling and comparison with experimental results

531 The orientation distributions needed for the analyti-  
532 cal model are extracted from the characterization of  
533 the fibre network measured with X-ray tomography.  
534 The mean fibre segment length is estimated from the  
535 mean diameters obtained with the SEM measure-  
536 ments. The transverse modulus is calculated accord-  
537 ing to Eq. 22 using the experimentally determined  
538 orientation distribution of the two sets of data. The  
539 transverse modulus is also determined experimen-  
540 tally by submitting stone wool and glass wool  
541  
542

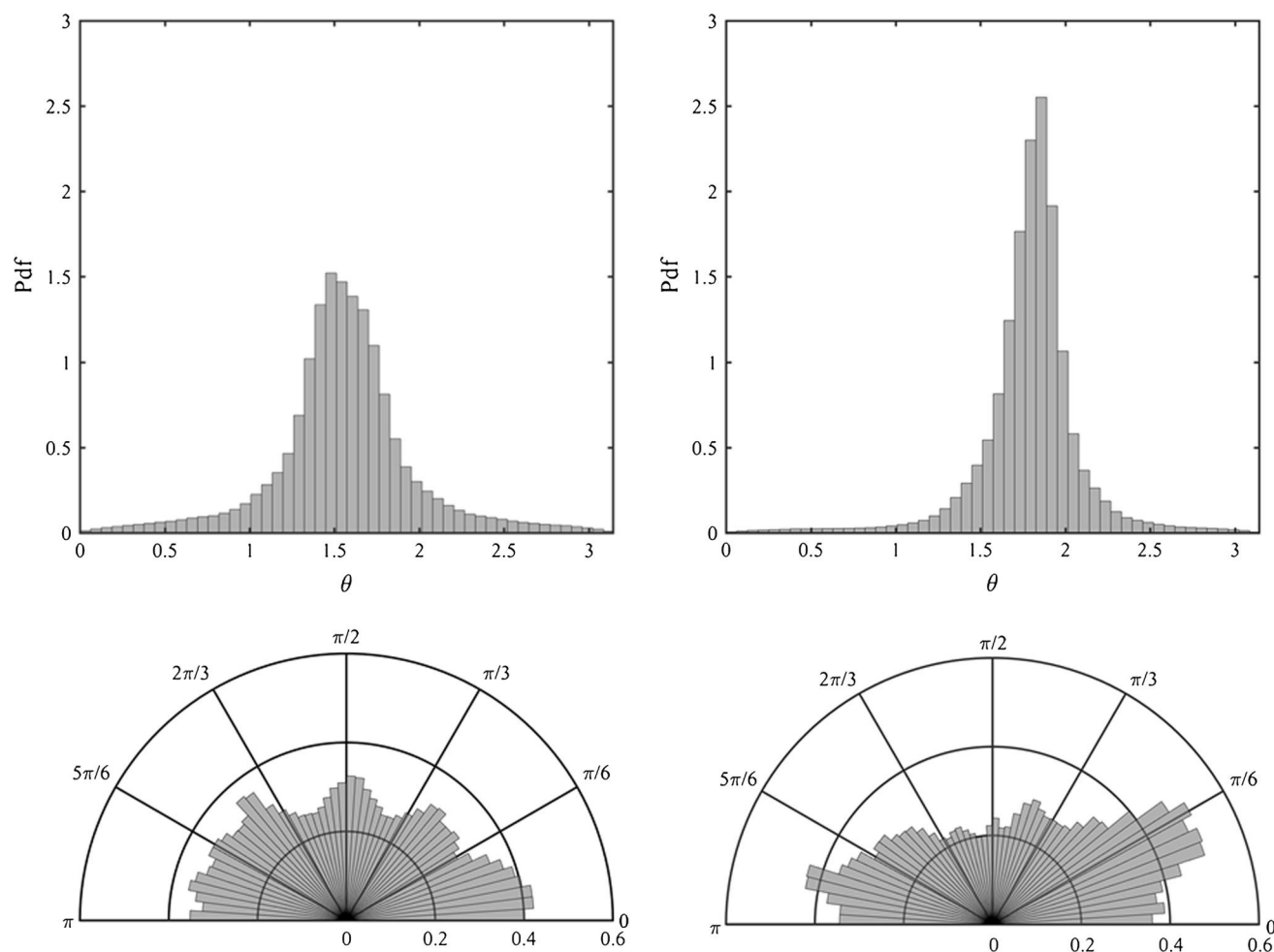


**Figure 2** Histogram plots of the angular distributions of elevation angles (top), azimuthal angles (bottom) for stone wool (left) and glass wool (right).

543 samples to a uniaxial compressive load in the thick-  
 544 ness direction of the product ( $z$  axis) and recording  
 545 the load as a function of the deflection. The samples  
 546 submitted to the compression testing originate from  
 547 the same products from which the samples for the  
 548 X-ray tomography characterization have been  
 549 extracted. The results along with the fibre volume  
 550 fraction are summarized in Table 3.

551 The predicted transverse moduli are substantially  
 552 close to the experimentally determined transverse  
 553 moduli, confirming that the main deformation  
 554 mechanism of the mineral wool fibre network is the  
 555 bending of the fibre segments between bonds. The  
 556 slight overestimation observed could be explained by  
 557 the overly rigid boundary conditions introduced at  
 558 the ends of each beam representing the fibre segment.

559 The lower transverse moduli of glass wool com-  
 560 pared to stone wool can be partly attributed to the

561 difference in the fibre orientation distribution  
 562 observed for the two materials. This result suggests  
 563 that the properties of mineral wool fibre network can  
 564 be tailored by controlling the fibre structure inside  
 565 the material and open rooms for optimization of  
 566 mineral wool products. The resolution of X-CT is  
 567 approximately up to 1 mm. However, the greyscale  
 568 analysis enabled more significant figures of the mean  
 569 fibre diameters and subsequently the predicted  
 570 transverse moduli.

## Conclusion

571  
 572 X-ray CT was used to investigate the fibre structure  
 573 of a glass wool and a stone wool sample. The struc-  
 574 ture tensor is employed to estimate the orientation  
 575 distribution of fibres, and a greyscale granulometry

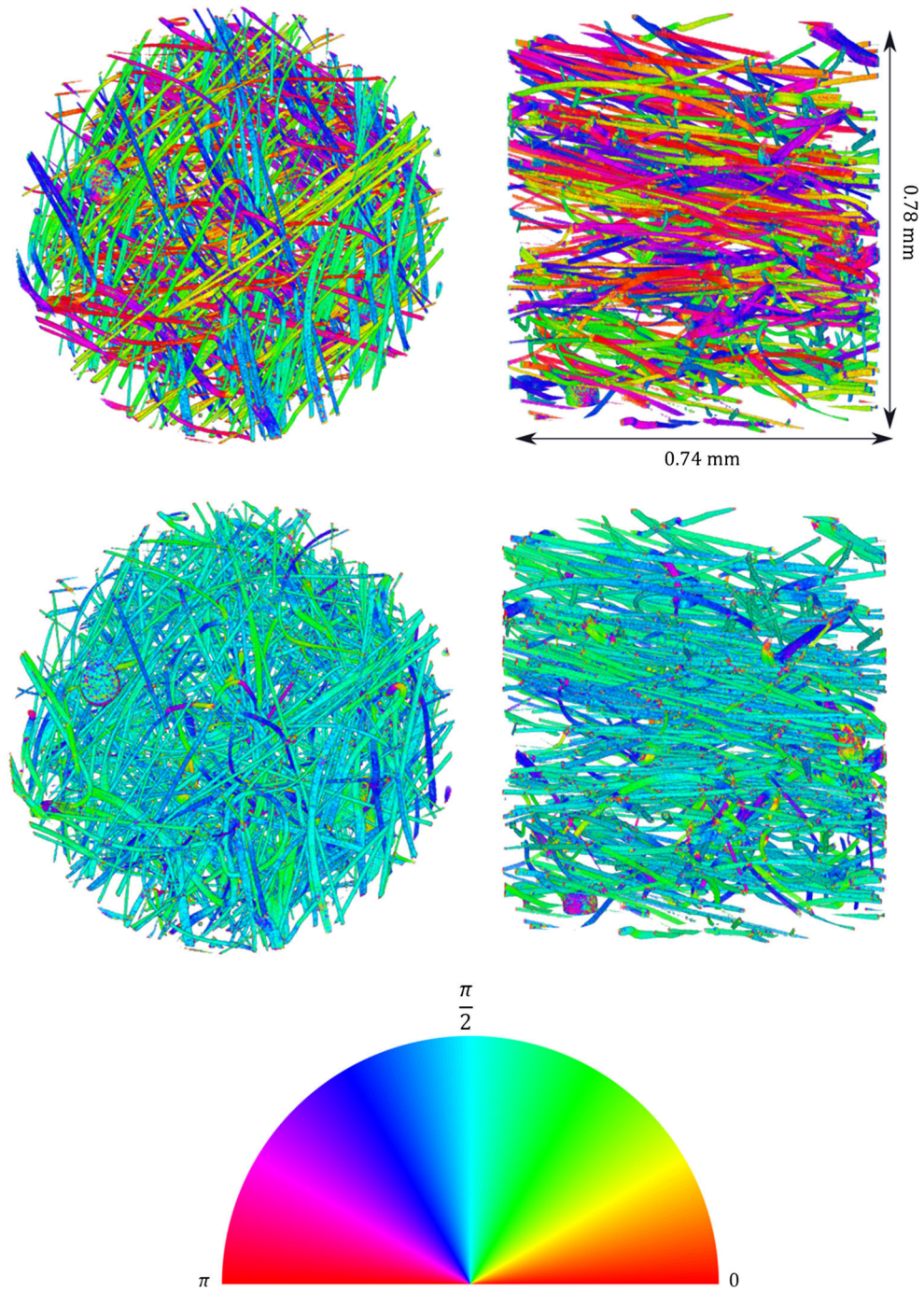


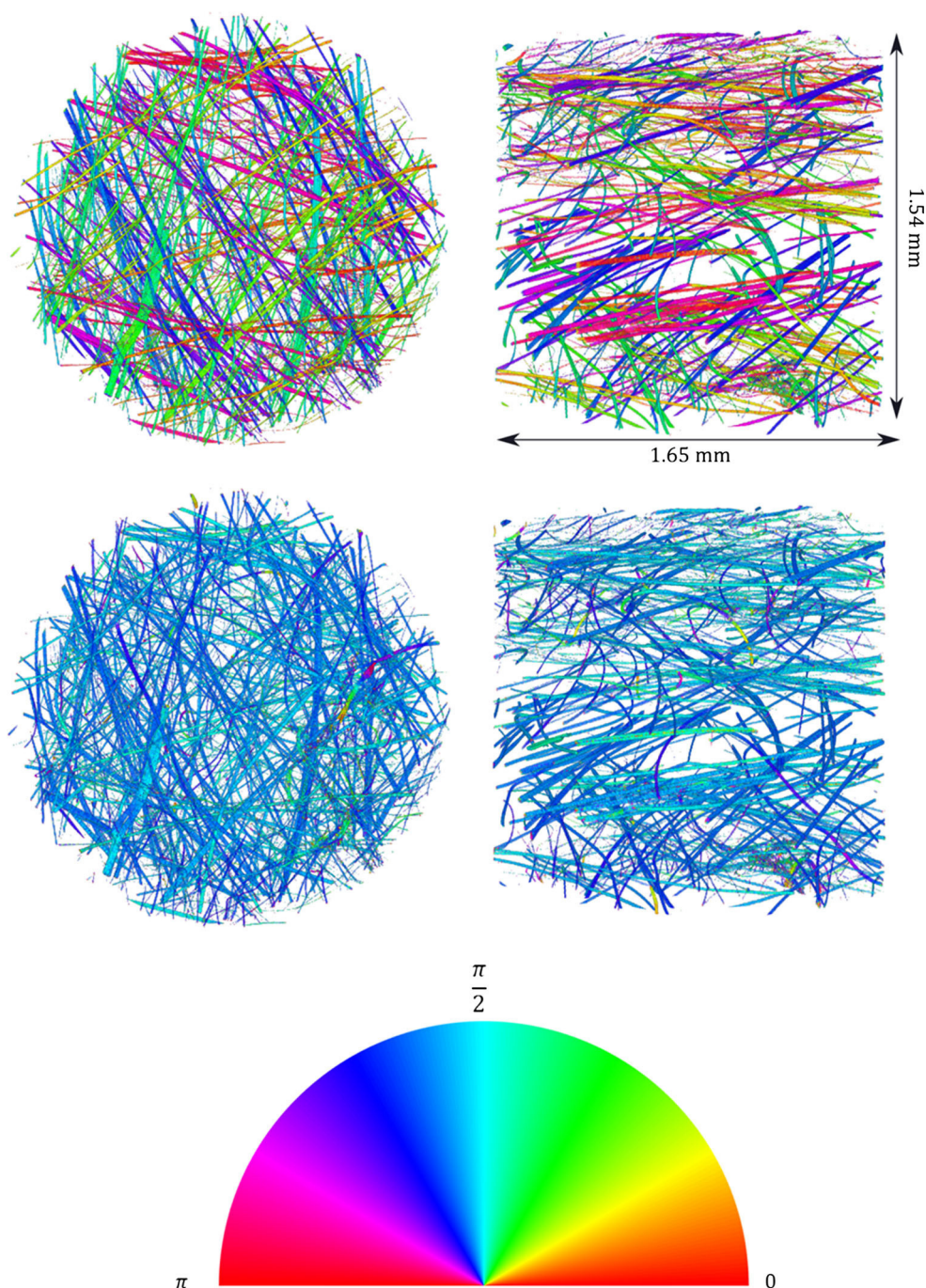
**Figure 3** 3D renderings of the angular variations of the stone wool fibres of azimuthal angles (top), elevation angles (bottom) displayed in the XY plane (left) and XZ plane (right).

576 method is applied to obtain the diameter distribution  
 577 of the fibres. The comparison of the distributions  
 578 returned by greyscale granulometry and 2D analysis  
 579 of SEM pictures shows that the analysis fails to  
 580 measure accurately the diameter of thin fibres. The  
 581 results of the image analysis indicate that both glass

wool and stone wool present some similarities in 582  
 their fibre structure, but the following main differ- 583  
 ences were noted: 584

- The fibres present a more planar structure in the 585  
 glass wool sample than in the stone wool sample. 586

**Figure 4** 3D renderings of the angular variations of the glass wool fibres of azimuthal angles (top), elevation angles (bottom) displayed in the  $XY$  plane (left) and  $XZ$  plane (right).



587 • The glass wool fibres present a wider distribution  
588 towards large diameters than the stone wool  
589 fibres.

590 The origin of the observed variation in the fibre ori-  
591 entation could be attributed to a different formation  
592 process of the fibre network for stone wool and glass  
593 wool.

The single deflection of a fibre segment is derived 594  
using the Euler–Bernoulli beam approximation. From 595  
there, the overall macroscopic stress and strain 596  
applied to the mineral wool fibre network are 597  
obtained and lead to an expression for the transverse 598  
modulus as a function of the fibre orientation distri- 599  
bution, Young’s modulus and volume fraction. 600

Using the orientation distribution, the transverse 601  
modulus of glass wool and stone wool is predicted. 602

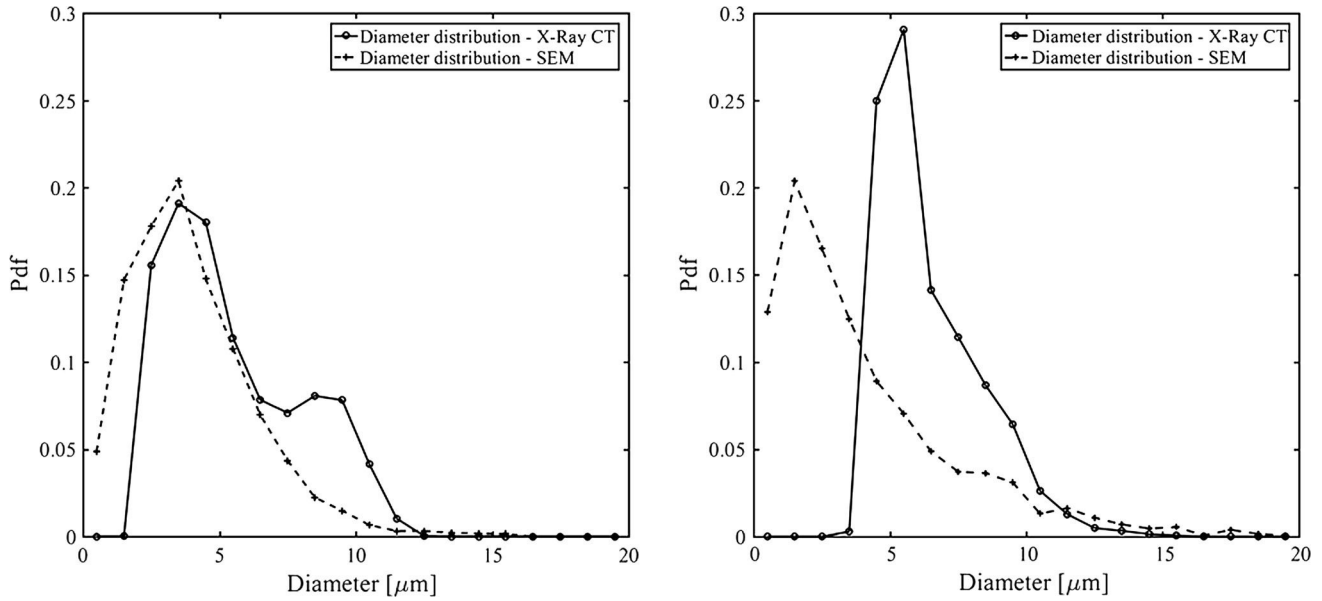


**Figure 5** Histogram plots of the fibre diameter distribution of stone wool (left) and glass wool (right).

**Table 3** Characteristics of the glass wool and the stone wool

	Glass wool	Stone wool
Fibre volume fraction (%)	0.86	0.90
Mean fibre diameter (μm)	4.11	4.01
Mean fibre segment length (mm)	1.80	1.64
Predicted transverse modulus (kPa)	1.28	3.18
Experimental transverse modulus (kPa)	1.40 ± 0.03	3.91 ± 0.20

603 The obtained values are in agreement with experi- 623  
 604 mental results confirming the assumption that the 624  
 605 main deformation mechanism of mineral wool is the 625  
 606 bending of the segment of fibres between bonds is 626  
 607 accurate. Furthermore, both the model and the 627  
 608 experimental results point out that glass wool is less 628  
 609 stiff than stone wool due to difference in the fibre 629  
 610 properties and arrangement in the material. The 630  
 611 methodology developed in this work provides new 631  
 612 descriptors to quantify the mineral wool product at a 632  
 613 microscopic scale. These new descriptors will help 633  
 614 explaining differences in product properties 634  
 615 observed from one factory line to another. For 635  
 616 example, different techniques are employed in the 636  
 617 ROCKWOOL Group to collect the fibres after the 637  
 618 fibre formation resulting in a different arrangement 638  
 619 of the fibres. The effect of the fibre collection can now  
 620 be quantified with the developed methodology.

621 Future studies will focus on obtaining a complete  
 622 characterization of mineral wool fibre networks using

X-Ray CT and image analysis. This will include  
 developing a fibre tracking method to estimate the  
 fibre length distributions as well as the density of  
 contacts between the fibres. The results of the char-  
 acterization will also be included in an improved  
 analytical model for the stiffness of mineral wool.

### Acknowledgements

629  
 630 Financial support from CINEMA: “the allianCe for  
 631 Imaging of Energy MATerials”, DSF-Grant No.  
 632 1305-00032B under “The Danish Council for Strategic  
 633 Research” and from Innovationsfonden is gratefully  
 634 acknowledged. The authors thank the 3D Imaging  
 635 Centre at The Technical University of Denmark for  
 636 the acquisition of the X-ray CT scans and Jesper  
 637 Asgaard Bøtner for helping with the SEM diameter  
 638 analyses.

639 **Compliance with ethical standards**

640 **Conflict of interest** The authors declare that there is  
641 no conflict of interest.

642 **References**

- 643 [1] Baudequin M, Ryschenkow G, Roux S et al (1999) Non-  
644 linear elastic behavior of light fibrous materials. *Eur Phys J B*  
645 *Condens Matter Complex Syst* 12:157–162. [https://doi.org/](https://doi.org/10.1007/s100510050990)  
646 [10.1007/s100510050990](https://doi.org/10.1007/s100510050990)
- 647 [2] Buffiere J-Y, Maire E, Adrien J et al (2010) In situ experi-  
648 ments with X ray tomography: an attractive tool for exper-  
649 imental mechanics. *Exp Mech* 50:289–305. [https://doi.org/](https://doi.org/10.1007/s11340-010-9333-7)  
650 [10.1007/s11340-010-9333-7](https://doi.org/10.1007/s11340-010-9333-7)
- 651 [3] James JP, Choi H-W, Pharoah JG (2012) X-ray computed  
652 tomography reconstruction and analysis of polymer elec-  
653 trolyte membrane fuel cell porous transport layers. *Int J*  
654 *Hydrog Energy* 37:18216–18230. [https://doi.org/10.1016/j.](https://doi.org/10.1016/j.ijhydene.2012.08.077)  
655 [ijhydene.2012.08.077](https://doi.org/10.1016/j.ijhydene.2012.08.077)
- 656 [4] Pfrang A, Didas S, Tsotridis G (2013) X-ray computed  
657 tomography of gas diffusion layers of PEM fuel cells: seg-  
658 mentation of the micro porous layer. *J Power Sour*  
659 235:81–86
- 660 [5] Tran H, Doumalin P, Delisee C et al (2012) 3D mechanical  
661 analysis of low-density wood-based fiberboards by X-ray  
662 microcomputed tomography and digital volume correlation.  
663 *J Mater Sci* 48:3198–3212. [https://doi.org/10.1007/s10853-](https://doi.org/10.1007/s10853-012-7100-0)  
664 [012-7100-0](https://doi.org/10.1007/s10853-012-7100-0)
- 665 [6] Maire E, Colombo P, Adrien J et al (2007) Characterization  
666 of the morphology of cellular ceramics by 3D image pro-  
667 cessing of X-ray tomography. *J Eur Ceram Soc*  
668 27:1973–1981. [https://doi.org/10.1016/j.jeurceramsoc.2006.](https://doi.org/10.1016/j.jeurceramsoc.2006.05.097)  
669 [05.097](https://doi.org/10.1016/j.jeurceramsoc.2006.05.097)
- 670 [7] Gaiselmann G, Manke I, Lehnert W, Schmidt V (2013)  
671 Extraction of curved fibers from 3D data. *Image Anal Stereol*  
672 32:57–63. <https://doi.org/10.5566/ias.v32.p57-63>
- 673 [8] Pandita S, Verpoest I (2003) Prediction of the tensile stiff-  
674 ness of weft knitted fabric composites based on X-ray  
675 tomography images. *Compos Sci Technol* 63:311–325.  
676 [https://doi.org/10.1016/S0266-3538\(02\)00253-1](https://doi.org/10.1016/S0266-3538(02)00253-1)
- 677 [9] Badel P, Sallé EV, Maire E, Boisse P (2009) Simulation and  
678 tomography analysis of textile composite reinforcement  
679 deformation at the mesoscopic scale. *Int J Mater Form*  
680 2:189–192. <https://doi.org/10.1007/s12289-009-0572-z>
- 681 [10] Pazmino J, Carvelli V, Lomov SV (2014) Formability of a  
682 non-crimp 3D orthogonal weave E-glass composite rein-  
683 forcement. *Compos Part A Appl Sci Manuf* 61:76–83.  
684 <https://doi.org/10.1016/j.compositesa.2014.02.004>
- [11] Zeng X, Brown LP, Endruweit A et al (2014) Geometrical  
modelling of 3D woven reinforcements for polymer com-  
posites: prediction of fabric permeability and composite  
mechanical properties. *Compos Part A Appl Sci Manuf*  
56:150–160. [https://doi.org/10.1016/j.compositesa.2013.10.](https://doi.org/10.1016/j.compositesa.2013.10.004)  
004
- [12] Straumit I, Lomov SV, Wevers M (2015) Composites: part A  
quantification of the internal structure and automatic gener-  
ation of voxel models of textile composites from X-ray  
computed tomography data. *Compos Part A* 69:150–158.  
<https://doi.org/10.1016/j.compositesa.2014.11.016>
- [13] Thibault X, Bloch J-F (2002) Structural analysis by X-Ray  
microtomography of a strained nonwoven papermaker felt.  
*Text Res J* 72:480–485. [https://doi.org/10.1177/](https://doi.org/10.1177/004051750207200603)  
004051750207200603
- [14] Vigié J, Latil P, Orgéas L et al (2013) Finding fibres and  
their contacts within 3D images of disordered fibrous media.  
*Compos Sci Technol* 89:202–210. [https://doi.org/10.1016/j.](https://doi.org/10.1016/j.compscitech.2013.09.023)  
compscitech.2013.09.023
- [15] Eberhardt CN, Clarke AR (2002) Automated reconstruction  
of curvilinear fibres from 3D datasets acquired by X-ray  
microtomography. *J Microsc* 206:41–53. [https://doi.org/10.](https://doi.org/10.1046/j.1365-2818.2002.01009.x)  
1046/j.1365-2818.2002.01009.x
- [16] Tausif M, Duffy B, Grishanov S et al (2014) Three-dimen-  
sional fiber segment orientation distribution using X-Ray  
microtomography. *Microsc Microanal* 20:1–10. [https://doi.](https://doi.org/10.1017/S1431927614000695)  
org/10.1017/S1431927614000695
- [17] Rolland du Roscoat S, Bloch J-F, Thibault X (2005) Syn-  
chrotron radiation microtomography applied to investigation  
of paper. *J Phys D Appl Phys* 38:A78–A84. [https://doi.org/](https://doi.org/10.1088/0022-3727/38/10A/015)  
10.1088/0022-3727/38/10A/015
- [18] Aronsson M (2002) Estimating fibre twist and aspect ratios  
in 3D voxel volumes. In: 16th International conference on  
pattern recognition
- [19] Rolland du Roscoat S, Decain M, Thibault X et al (2007)  
Estimation of microstructural properties from synchrotron  
X-ray microtomography and determination of the REV in  
paper materials. *Acta Mater* 55:2841–2850. [https://doi.org/](https://doi.org/10.1016/j.actamat.2006.11.050)  
10.1016/j.actamat.2006.11.050
- [20] Marulier C, Dumont PJJ, Orgéas L et al (2012) Towards 3D  
analysis of pulp fibre networks at the fibre and bond levels.  
*Nord Pulp Pap Res J Pap Phys* 28:245–255
- [21] Marulier C, Dumont PJJ, Orgéas L et al (2015) 3D analysis  
of paper microstructures at the scale of fibres and bonds.  
*Cellulose* 22:1517–1539. [https://doi.org/10.1007/s10570-](https://doi.org/10.1007/s10570-015-0610-6)  
015-0610-6
- [22] Geiss RH, Rice KP, Keller RR et al (2009) Three dimen-  
sional analysis of a compression test on stone wool. *Acta*  
*Mater* 57:3310–3320

- 734 [23] Maire E, Adrien J, Hild F, et al (2013) Digital X-ray  
735 tomography volume correlation of Rockwool during com-  
736 pression. In: Conference Proceedings of the society for  
737 experimental mechanics, pp 291–298
- 738 [24] Couprie M, Meulenyzer S, Salem MA et al (2014) Fibre  
739 analysis in 3D materials and process validation on artificial  
740 data. *J Microsc* 255:78–88. <https://doi.org/10.1111/jmi.12138>  
741
- 742 [25] Tan JC, Elliott JA, Clyne TW (2006) Analysis of tomogra-  
743 phy images of bonded fibre networks to measure distribu-  
744 tions of fibre segment length and fibre orientation. *Adv Eng*  
745 *Mater* 8:495–500. <https://doi.org/10.1002/adem.200600033>  
746
- 747 [26] Gibson LJ, Ashby MF, Schajer GS, Robertson CI (1982) The  
748 Mechanics of Two-Dimensional Cellular Materials. *Proc R*  
749 *Soc Lond A Math Phys Eng Sci* 382:25–42
- 750 [27] Mezeix L, Bouvet C, Huez J, Poquillon D (2009) Mechan-  
751 ical behavior of entangled fibers and entangled cross-linked  
752 fibers during compression. *J Mater Sci* 44:3652–3661.  
753 <https://doi.org/10.1007/s10853-009-3483-y>  
754
- 755 [28] Clyne TW, Markaki AE, Tan JC (2005) Mechanical and  
756 magnetic properties of metal fibre networks, with and  
757 without a polymeric matrix. *Compos Sci Technol*  
758 65:2492–2499. <https://doi.org/10.1016/j.compscitech.2005.05.037>  
759
- 760 [29] Bigun J, Granlund GH, Wiklund J (1991) Multidimensional  
761 orientation estimation with applications to texture analysis  
762 and optical flow. *IEEE Trans Pattern Anal Mach Intell*  
763 13:775–790. <https://doi.org/10.1109/34.85668>  
764
- 765 [30] Weickert J (1995) Multiscale texture enhancement. In: Pro-  
766 ceedings computer analysis of images and patterns, 6th  
767 international conference, CAIP'95 Prague, Czech Republic,  
768 Sept 6–8, 1995, pp 230–237
- 769 [31] Köthe U (2003) Edge and junction detection with an  
770 improved structure tensor. *Ger Assoc Pattern Recognit.*  
771 [https://doi.org/10.1007/978-3-540-45243-0\\_4](https://doi.org/10.1007/978-3-540-45243-0_4)  
772
- 773 [32] Budde MD, Frank JA (2012) Examining brain microstruc-  
774 ture using structure tensor analysis of histological sections.  
775 *Neuroimage* 63:1–10. <https://doi.org/10.1016/j.neuroimage.2012.06.042>  
776
- 777 [33] Van Vliet LJ, Faas FGA (2006) Multi-orientation analysis by  
778 decomposing the structure tensor and clustering. *Proc Int*  
779 *Conf Pattern Recognit* 3:856–860. <https://doi.org/10.1109/ICPR.2006.829>  
780
- 781 [34] Scharr H, Black MJ, Haussecker H (2003) Image statistics  
782 and anisotropic diffusion. In: Proceedings ninth IEEE  
783 international conference on computer vision, vol 2. IEEE,  
784 pp 840–847
- 785 [35] Moreno R, Borga M (2012) Estimation of trabecular thick-  
786 ness in gray-scale images through granulometric analysis. In:  
787 SPIE 8314: medical imaging. San Diego  
788
- 789 [36] Standfest G, Kranzer S, Petutschnigg A, Dunky M (2010)  
790 Determination of the microstructure of an adhesive-bonded  
791 medium density fiberboard (MDF) using 3-D sub-microm-  
792 eter computer tomography. *J Adhes Sci Technol*  
793 24:1501–1514. <https://doi.org/10.1163/016942410X501052>  
794
- 795 [37] Peyrega C, Jeulin D, Delisée C, Lux J (2009) 3D morpho-  
796 logical modelling of a random fibrous network. *Image Anal*  
797 *Stereol* 28:129–141
- 798 [38] Lux J, Ahmadi A, Gobbé C, Delisée C (2006) Macroscopic  
799 thermal properties of real fibrous materials: volume averag-  
800 ing method and 3D image analysis. *Int J Heat Mass Transf*  
801 49:1958–1973. <https://doi.org/10.1016/j.ijheatmasstransfer.2005.09.038>  
802
- 803 [39] Redenbach C, Vecchio I (2011) Statistical analysis and  
804 stochastic modelling of fibre composites. *Compos Sci*  
805 *Technol* 71:107–112. <https://doi.org/10.1016/j.compscitech.2010.10.014>  
806
- 807 [40] Komori T, Makishima K (1979) Geometrical expressions of  
808 spaces in anisotropic fiber assemblies. *Text Res J*  
809 49:550–555. <https://doi.org/10.1177/004051757904900912>  
810
- 811 [41] Komori T, Makishima K (1977) Numbers of fiber-to-fiber  
812 contacts in general fiber assemblies. *Text Res J* 47:13–17.  
813 <https://doi.org/10.1177/004051757704700104>  
814
- 815 [42] Makishima A, Mackenzie JD (1975) Calculation of bulk  
816 modulus, shear modulus and Poisson's ratio of glass. *J Non*  
817 *Cryst Solids* 17:147–157. [https://doi.org/10.1016/0022-3093\(75\)90047-2](https://doi.org/10.1016/0022-3093(75)90047-2)  
818
- 819 [43] Koenig AR, Hamilton RD, Laskowski TE et al (1993) Fiber  
820 diameter measurement of bulk man-made vitreous fiber.  
821 *Anal Chim Acta* 280:289–298. [https://doi.org/10.1016/0003-2670\(93\)85133-5](https://doi.org/10.1016/0003-2670(93)85133-5)  
822

Journal : **10853**  
Article : **2044**

## Author Query Form

**Please ensure you fill out your response to the queries raised below and return this form along with your corrections**

Dear Author

During the process of typesetting your article, the following queries have arisen. Please check your typeset proof carefully against the queries listed below and mark the necessary changes either directly on the proof/online grid or in the 'Author's response' area provided below

Query	Details Required	Author's Response
<a href="#">AQ1</a>	Please check and confirm the author name near the reference citations [26, 28, 29].	
<a href="#">AQ2</a>	Please confirm the section headings are correctly identified.	
<a href="#">AQ3</a>	Please check and confirm the inserted citation of Fig. 5 is correct. If not, please suggest an alternative citation. Please note that figures should be cited in sequential order in the text.	
<a href="#">AQ4</a>	Please check the clarity of the phrase 'the SEM based are' in the sentence 'As the distribution of the fibres diameter...fibres at their medial axis'.	